Planetary and Space Science 59 (2011) 1829–1841

Contents lists available at ScienceDirect

Planetary and Space Science

journal homepage: www.elsevier.com/locate/pss

Analysis of MESSENGER Gamma-Ray Spectrometer data from the Mercury flybys

Edgar A. Rhodes [a,*], Larry G. Evans [b], Larry R. Nittler [c], Richard D. Starr [d], Ann L. Sprague [e], David J. Lawrence [a], Timothy J. McCoy [f], Karen R. Stockstill-Cahill [f], John O. Goldsten [a], Patrick N. Peplowski [a], David K. Hamara [e], William V. Boynton [e], Sean C. Solomon [c]

[a] Johns Hopkins University Applied Physics Laboratory, Laurel, MD 20723, USA
[b] Computer Sciences Corporation, Lanham, MD 20706, USA
[c] Department of Terrestrial Magnetism, Carnegie Institution of Washington, Washington, DC 20015, USA
[d] The Catholic University of America, Washington, DC 20064, USA
[e] Lunar and Planetary Laboratory, The University of Arizona, Tucson, AZ 85721, USA
[f] Smithsonian National Museum of Natural History, Washington, DC 20560, USA

ARTICLE INFO

Article history:
Received 6 December 2010
Received in revised form
11 July 2011
Accepted 15 July 2011
Available online 4 August 2011

Keywords:
Mercury
Gamma-ray spectrometry
Elemental abundances
MESSENGER

ABSTRACT

During its three flybys of Mercury, the MESSENGER spacecraft made the first detection of gamma-ray emission from the planet's surface. With a closest approach distance of ~200 km, the flybys provided an opportunity to measure elemental abundances of Mercury's near-equatorial regions, which will not be visited at low altitude during MESSENGER's orbital mission phase. Despite being limited by low planetary photon flux, sufficient counts were accumulated during the first two flybys to estimate bounds on abundances for some elements having relatively strong gamma-ray spectral peaks, including Si, Fe, Ti, K, and Th. Only for Si is the standard deviation σ sufficiently small to conclude that this element was detected with 99% confidence. Iron and potassium are detected at the $2-\sigma$ (95% confidence) level, whereas only upper bounds on Ti and Th can be determined. Relative to a Si abundance assumed to be 18 weight percent (wt%), $2-\sigma$ upper bounds have been estimated as 9.7 wt% for Fe, 7.0 wt% for Ti, 0.087 wt% for K, and 2.2 ppm for Th. The relatively low upper bound on K rules out some previously suggested models for surface composition for the regions sampled. Upper bounds on Fe/Si and Ti/Si ratios are generally consistent with Ti and Fe abundances estimated from the analysis of measurements by the MESSENGER Neutron Spectrometer during the flybys but are also permissive of much lower concentrations.

1. Introduction

The surface composition of Mercury provides critical clues to the origin and evolution of the planet (Boynton et al., 2007). The Gamma-Ray Spectrometer (GRS) on the MErcury Surface, Space ENvironment, GEochemistry, and Ranging (MESSENGER) spacecraft, one of two sensors that comprise the Gamma-Ray and Neutron Spectrometer (GRNS) instrument (Goldsten et al., 2007), uses a mechanically cryocooled germanium detector to measure spectra of gamma rays emanating from the planet's surface as a result of cosmic-ray interactions and radioactive decay. Elemental abundances can be determined by analyzing these spectra. The MESSENGER spacecraft has flown by Mercury three times on its way to a planned orbit insertion in March 2011 (Solomon et al., 2007). The first flyby (M1) occurred on 14 January 2008, the second (M2) on 6 October 2008, and the third (M3) on 29 September 2009. The Mercury flybys had a closest approach distance of ~200 km near the equator and thus provide the opportunity to measure surface elemental abundances of near-equatorial regions, which will not be visited at low altitude during the mission orbital phase. Unfortunately, the spectra are limited by low planetary photon flux and the short time available at low altitude. During the mission orbital phase, counting statistics will be improved by accumulating counts for numerous orbits over a given surface region, but each flyby is equivalent to only a single orbit. Sufficient counts have nonetheless been accumulated during the first two flybys to estimate bounds on abundances for some elements having relatively strong spectral peaks, including Si, Fe, Ti, and K. During the third flyby, the spacecraft experienced a safe-hold demotion shortly before closest approach, so no abundance estimates were obtained for that encounter.

A cutaway model of the GRS sensor assembly is shown in Fig. 1. The sensor consists of an N-type coaxial Ge crystal of diameter 5 cm and length 5 cm, inside a cryostat having nested gold-plated shields, surrounded on the sides and back by a borated-plastic (BC454) scintillator that acts as an anticoincidence shield to reject

* Corresponding author. Tel.: +202 238 3829.
E-mail address: Ed.Rhodes@jhuapl.edu (E.A. Rhodes).

0032-0633/$ - see front matter © 2011 Elsevier Ltd. All rights reserved.
doi:10.1016/j.pss.2011.07.018

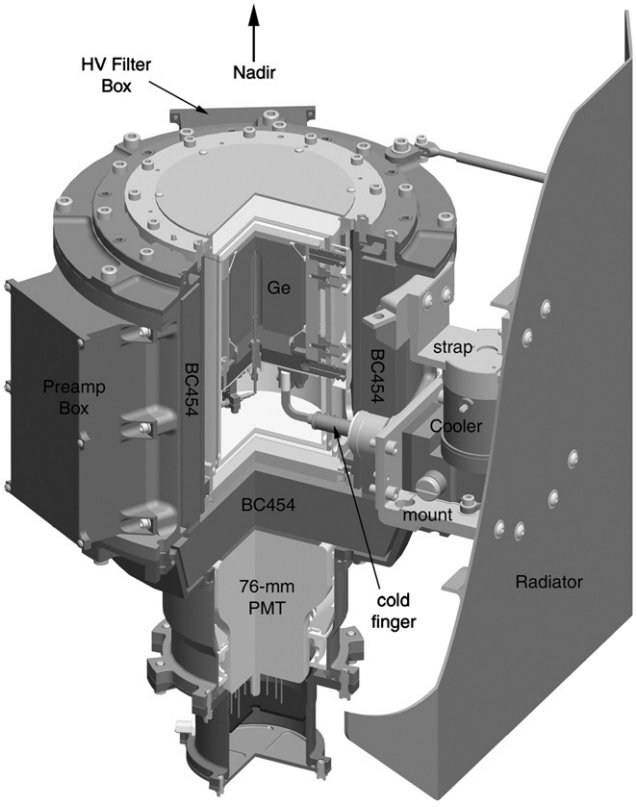

Fig. 1. Cutaway CAD drawing of the MESSENGER GRS sensor, showing the Ge cryostat and borated-plastic (BC454) detector assemblies along with the cryocooler and its passive radiator. The abbreviations "HV" and "PMT" denote "high voltage" and "photomultiplier tube," respectively.

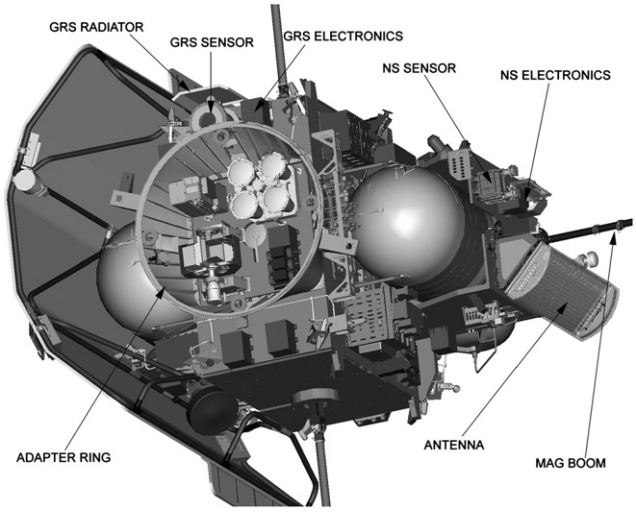

Fig. 2. CAD drawing showing the positions of GRS and NS on the MESSENGER spacecraft. Only a portion of the 3.6-m boom for MESSENGER's Magnetometer (MAG) is shown. Also indicated are one of MESSENGER's two high-gain phased-array antennas and the adapter ring by which the spacecraft was mated to the upper stage of the launch vehicle.

cosmic rays (Goldsten et al., 2007). The Ge crystal is cooled to 90 K operating temperature by a rotary Stirling cryocooler that rejects its heat to a passive radiator. The nadir direction points along the main spacecraft axis. The positions of the GRS, the Neutron Spectrometer (NS) sensor on GRNS, and other subsystems on the spacecraft are shown in Fig. 2. Ideally, the spacecraft would normally point towards the planet center for the best view by the instruments,

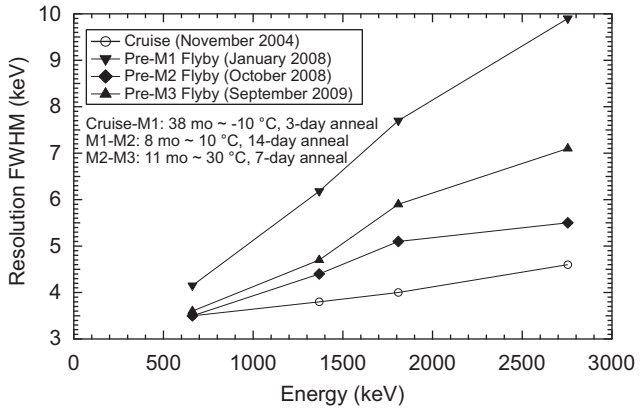

Fig. 3. History of MESSENGER GRS energy resolution (expressed as FWHM), temperature, and annealing.

unless it must rotate so that the sunshade (shown on the left in Fig. 2) can continue to shield the spacecraft from the Sun. The cryocooler has a limited lifetime, so it was turned off between the flybys. It was then brought into operation for each flyby in time for annealing of the Ge crystal followed by a background measurement of up to 36 h prior to closest approach. The annealings raised the Ge temperature to 84 °C to improve energy resolution degraded by radiation damage from cosmic rays, with different annealing times for each flyby. Long, slow annealings at lower temperatures during cruise were also employed. Energy resolution was measured for a range of strong peaks in the spectra during each flyby background measurement and during the initial cruise test. The history of energy resolution versus annealing is shown in Fig. 3. As can be seen, of the three flybys, M2 had the best energy resolution due to the 14-day annealing period prior to the flyby.

2. Flyby parameters

As the spacecraft approached the planet at altitudes less than about 5000 km during each flyby, a significant count rate from gamma rays emitted by the planetary surface, compared to spacecraft background, began to be registered by the spectrometer. This signal-to-background ratio improved as the altitude decreased. The question arises as to the maximum altitude to include in summing the GRS closest-approach counting intervals in order to maximize the signal-to-background ratio while maintaining good counting statistics. Preliminary analysis with maximum summing altitudes of 5000, 2500, and 1000 km indicated that summing up to 2500 km provides the lowest errors in abundances of these three choices. The footprint of the planet surface from which planetary gamma rays can be detected becomes smaller with decreasing spacecraft altitude. The spectrometer will detect planetary gamma rays from limb to limb, but response is low near the limbs and peaks for surface areas close to the sub-spacecraft point. Shown in Fig. 4 is a succession of instantaneous footprints spaced ~2 min apart and delineating the full width at half maximum (FWHM) of the footprint response below 2500 km altitude for the second flyby, yielding a characteristic "bow-tie" shape with a minimum at the closest approach distance of ~200 km. The footprint centers extended from 164°E longitude at 2500 km altitude through 229°E at closest approach to 294°E at 2500 km altitude, all at near-equatorial latitudes.

Flight parameters as functions of time from closest approach for the second Mercury flyby, including altitude, solid angle subtended by the spacecraft, and the angle of the instrument boresight with respect to nadir, are shown in Fig. 5a. Only 24 min was spent below 2500 km altitude. Note that very little time was

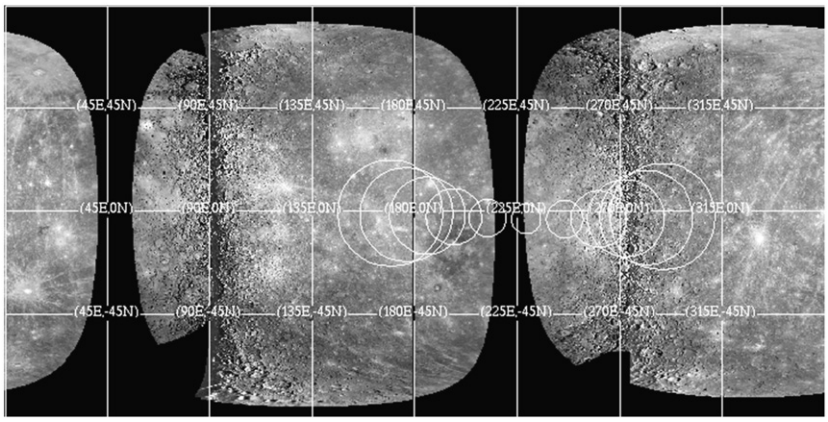

Fig. 4. GRS footprints on Mercury during M2. Each circle represents a snapshot every ~2 min as the spacecraft traveled from 2500 km altitude down to 200 km closest-approach distance and back to 2500 km altitude. The diameter of each circle is approximately the full width at half maximum of the GRS spatial response at a specific altitude and time. The background mosaic is derived from MESSENGER Mercury Dual Imaging System M1 and M2 images.

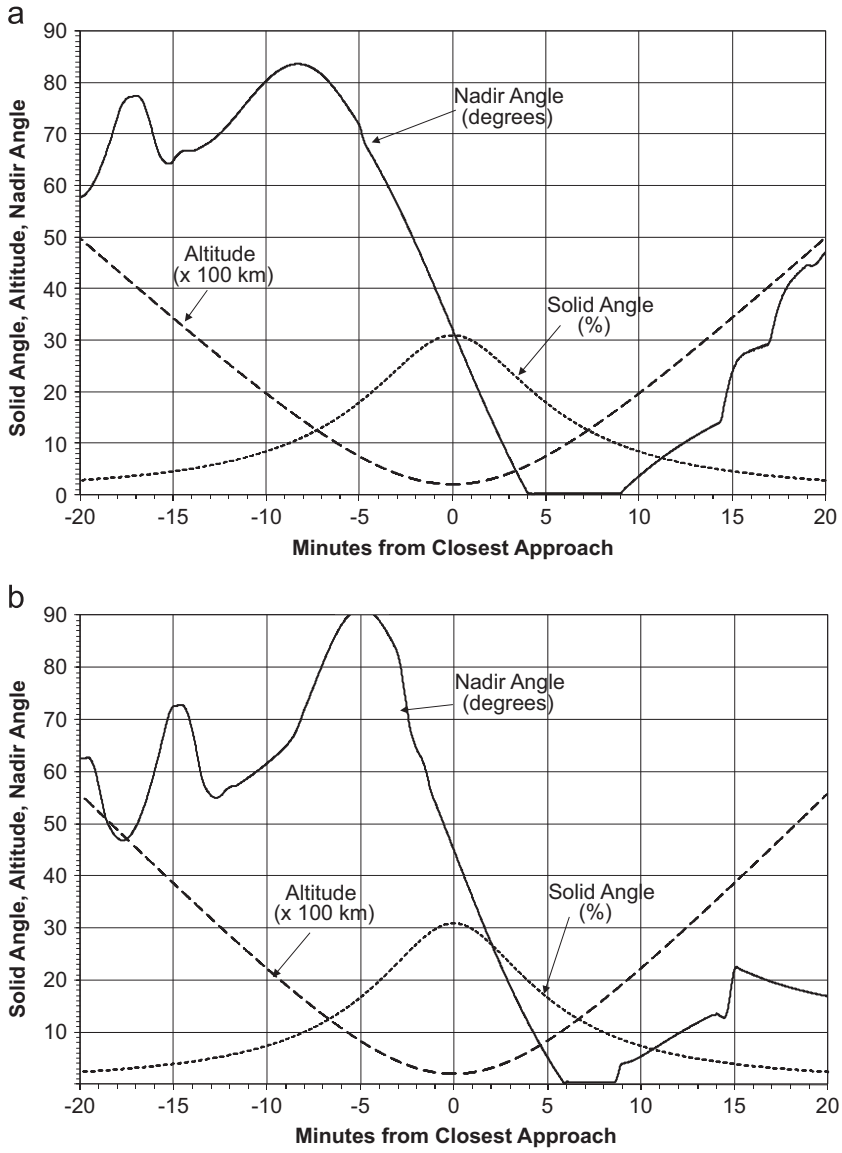

Fig. 5. Flight parameters important to GRS during (a) M2 and (b) M1. Solid angle is given as a percentage of the maximum of 4π sr. Closest-approach data are summed over time periods when the altitude is less than 2500 km (corresponding to a period of ~12 min for M2 and ~11 min for M1 spanning closest approach).

spent with the GRS pointing near nadir, but a substantial fraction of time was spent near 90°, so the GRS was observing the planet through its side shield (see Figs. 1 and 2) for much of the flyby time. This far-off-nadir spacecraft orientation was necessary to ensure that the sunshade shielded the spacecraft from the Sun. Flight parameters for the first flyby were similar (Fig. 5b), except that the time spent at less than 2500 km altitude was 22 min, and even less time was spent pointing near nadir than for the second flyby. The "bow-tie" footprint shape for the first flyby is thus slightly contracted from that shown in Fig. 4; the footprint centers extended from 334°E longitude at 2500 km altitude through 360° to 38°E at closest approach to 102°E at 2500 km altitude, all at near-equatorial latitudes. Thus, the two flybys encountered opposite sides of the planet, with minimal overlap, and they provide elemental abundance information for essentially two different equatorial regions of Mercury's surface.

3. GRS elemental abundance measurements during the flybys

Because Mercury has almost no atmosphere to absorb galactic cosmic rays (GCRs), nor a sufficiently strong magnetic field to deflect them, GCRs continuously bombard and penetrate its surface and create many secondary nuclear particles, among them energetic neutrons. These neutrons interact with nuclei in crustal materials to create gamma rays of discrete energies characteristic of a given element, either through a process of inelastic scattering of fast neutrons or by capture of neutrons that have moderated to thermal energies through elastic scattering. Additionally, radioisotopes of K, Th, and U in the crust emit gamma rays during radioactive decay. Most of the gamma rays downscatter to lower energies and become a source of background continuum, but a fraction of these gamma rays escape uncollided to space, where they can be detected. Gamma rays with energies up to ~10 MeV emanate from depths of about 10–20 cm beneath the surface, depending on the crustal density and elemental composition (Reedy, 1978).

The MESSENGER Gamma-Ray Spectrometer was ground-calibrated for detection efficiency as a function of energy and incidence angle. These efficiencies, the detector active area, and the solid angle at altitude then allow the peak fluxes at the planet surface to be determined from the peak counts in the gamma-ray spectrum. With the relevant neutron-reaction and gamma-ray-production cross-sections, radiation transport codes are used to model the production and transport of secondary nuclear particles from GCRs for an assumed crustal surface composition and compute the discrete gamma-ray fluxes emitted from the surface. Comparison of the computed discrete gamma-ray fluxes with the corresponding measured peak fluxes allows determination of the surface elemental composition. Abundances of radioactive isotopes can be determined from measured gamma-ray fluxes and the known decay lifetimes, if an average surface composition is assumed.

There are several important complications to this procedure. First, the spacecraft is also bombarded with GCRs, which create background gamma rays from the same elements in the spacecraft as may be on the planetary surface. This background is determined by averaging the GRS spectra acquired at high altitude prior to the each flyby, and it must be subtracted from the flyby spectra acquired below ~2500 km altitude. Second, as the spacecraft approaches the planet, the GCR flux at the spacecraft decreases due to shadowing by the planet, but the flux of fast and thermal neutrons arising from GCR interactions in the planet increases at the spacecraft, resulting in a net amplification of the background that varies with spacecraft altitude and attitude. Thus, the pre-flyby background count rate in each gamma-ray peak of interest (except for those from radioactive isotopes, for which there is no background amplification) must be corrected for this amplification before subtracting from the low-altitude average peak count rate. A final complication for the flybys is that the spacecraft orientation changed during the approach to the planet at low altitude and was far off nadir on average (see Fig. 5). This change in orientation requires calculation of the attenuation by the spacecraft and GRS components of the planetary gamma rays as a function of attitude angles, as well as knowledge of the Ge detector efficiency at these attitude angles. A factor not considered here is the variation in GCR flux magnitude and spectrum with distance from the Sun and with solar activity, which causes count-rate variation in the gamma-ray peaks.

4. Analysis of flyby spectra

For the short-duration flybys, gamma-ray peak analysis has been restricted to energies less than ~3 MeV, for which the

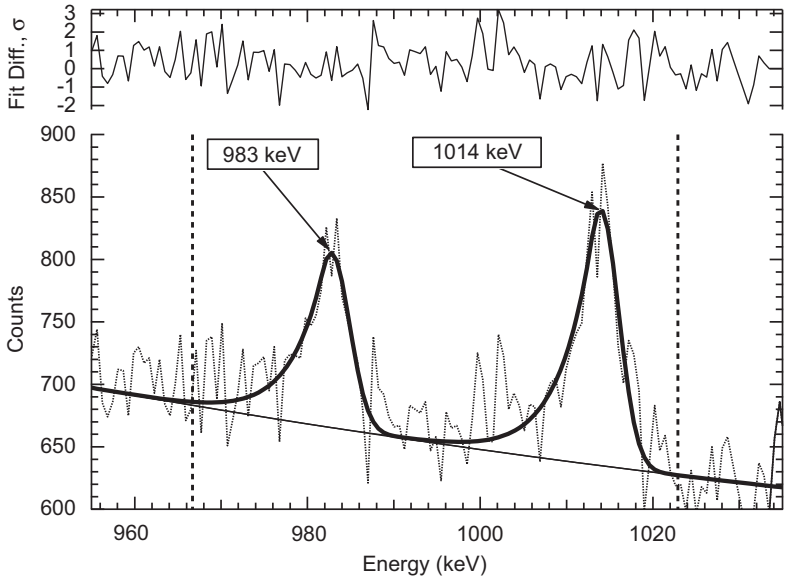

Fig. 6. Fit of the Ti 983 keV and Al 1014 keV peaks to the M1 high-altitude GRS background spectrum. Peaks are fit to the region between the vertical dashed lines. The baseline is fit to a larger region not shown in this figure. The smooth lines show the fit, and the dotted lines denote the measurements. The upper plot is the difference between the fit and the measurements in units of standard deviation (as derived from count statistics), labeled as "Fit Diff., σ".

Ge detector has sufficient efficiency to obtain reasonable count statistics. Gamma-ray peaks chosen for analysis are for a set of elements important to the bulk composition of Mercury and needed for element abundance normalization for which the peaks are relatively strong, including Ti at 983 keV, Fe at 847 keV, Si at 1779 keV, ^{40}K at 1461 keV, and ^{232}Th at 2615 keV. These peaks all come from inelastic scattering of fast neutrons, except for K and Th, which come from natural radioactivity. Two methods have been used to analyze the spectra from M1 and M2. One method is to sum the spectra together from both flybys for the background and flyby measurement segments and then subtract the background. The second method is to subtract the background from the flyby segment for each flyby separately, and then average the result. Note that the energy resolution is substantially broader for the first flyby (Fig. 3) and has more low-energy tailing. The first method makes it easier to identify and analyze peaks and yields a faster analysis. This method was followed for Si, which is not expected to vary strongly over the planet, and for K and Th, whose peaks are too weak to identify in the time-constrained low-altitude spectra unless the spectra are added together. The second method preserves the peak shapes for both flybys (adhering strictly to the spectrum-fitting model) and yields surface element abundances that may differ for the two regions sampled. The second method will be illustrated here for Ti and Fe. The two methods yielded similar results within count statistics for Ti, Fe, and Si. The analysis for Si and K has been presented previously (Evans et al., 2008), as has that for Ti and Fe (Rhodes et al., 2009).

The GRS spectra are summed over the high-altitude pre-flyby regions and the closest-approach altitudes and then analyzed using software that performs a nonlinear least-squares fit of the spectra sums to peaks, each defined by a Gaussian function (spliced to an exponential tail on the low-energy side) and a continuum background specified by a low-degree polynomial. The fit provides an error analysis of the fit parameters and peak areas. The peak area gives the counts associated with a given peak. The peaks can overlap; peak width, height, energy position, and exponential-tail splicing position can be fixed or determined from the fit; and the background polynomial degree can be fixed. Background is first fit to regions outside the peaks and is fixed during the peak fitting; this procedure was found to be the best

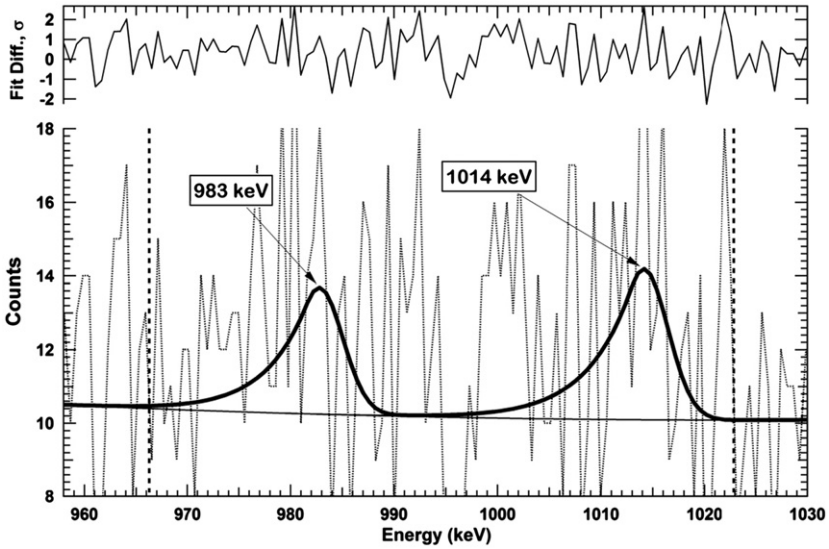

Fig. 7. Fit of the Ti 983 keV and Al 1014 keV peaks to the M1 GRS closest-approach (<2500 km altitude) spectrum. Peaks are fit to the region between the vertical dashed lines with the same peak shape parameters as those used in Fig. 6. The baseline is fit to a larger region not shown in this figure. Other particulars are as in Fig. 6.

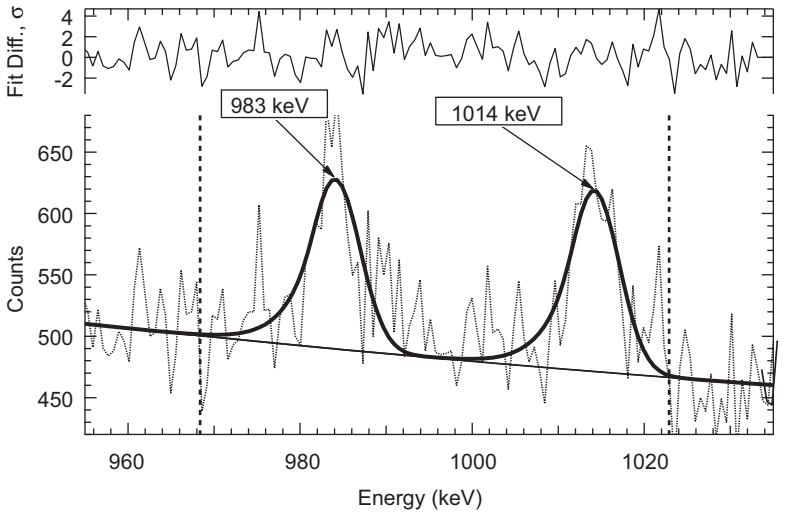

Fig. 8. Fit of the Ti 983 keV and Al 1014 keV peaks to the M2 high-altitude GRS background spectrum. Peaks are fit to the region between the vertical dashed lines. The baseline is fit to a larger region not shown in this figure. Other particulars are as in Fig. 6.

fitting option. Peak shapes and energy positions determined for the pre-flyby spectral sums are also used for the closest-approach spectral sums for a given flyby; only the peak heights are determined for the closest-approach fit. This procedure limits the fit statistical error for the time-limited closest-approach spectra and is appropriate because only the peak heights should differ for the two spectral sums. (Any gain change is minimal because the spectra are corrected for temperature.)

The GRS spectra prior to and during M1 closest approach (CA, at less than 2500 km altitude) are shown for the region of the 983-keV Ti peak in Figs. 6 and 7, respectively. Included in the peak fits is the inelastic Al peak at 1014 keV, to extend the baseline so as to more accurately measure the background continuum. The corresponding spectra for M2 are shown in Figs. 8 and 9. The Al peak count rate ratio of the flyby to pre-flyby measurement can be used as a measure of the background amplification factor, because the Al peak flux from the large mass of Al in the instrument is likely much larger than that from the planetary surface. However, there is a possible time-varying peak component from ^{27}Mg, which decays with a 9.46-min half-life, emitting a gamma ray of the same energy, 1014 keV. ^{27}Mg can be produced from fast neutrons by the (n,p) reaction in Al and from thermal neutron capture in Mg (there is a substantial mass of Mg in the GRS). The effect of this time variation is small compared to count statistical error and has been ignored. The count rate analysis obtained from the peaks shown in Figs. 6–9 is given in Table 1. The reported count rate errors are simply the standard deviation σ derived from count statistics.

The small net Al count rate supports the hypothesis that the GRS Al signal dwarfs that from any Al in the planet. The ratio of peak-area Al flux during CA to that from the pre-CA background is 2.40 ± 0.73 for M1 and 1.80 ± 0.67 for M2, with an average of 2.10 ± 0.49 $(1-\sigma)$. For simplicity, we round the average peak-area ratio for the two flybys to 2 and take this to be a constant amplification factor for correcting the inelastic scatter peaks of Ti, Fe, and Si. We do not consider the counting statistical error in this Al background amplification factor, because it may in fact be close to 2 with much better accuracy than indicated by the GRS count statistics (Table 1). An average value of 2.13, very close to the 2.10 average above, is obtained by calculations of the amplification factor using the MESSENGER NS borated-plastic fast-neutron detector flyby spectra multiplied by the Al neutron inelastic scattering gamma-ray-production cross-section. This detector provides a much higher count rate (and much better count statistics) than the GRS Ge detector. However there is some systematic error due to the NS placement at a different spacecraft location than the GRS. One could also consider allowing for some Al contribution from the planet, which would reduce the Al background amplification factor. Allowing 3 wt% Al for Mercury surface material from the "preferred" compositional model of

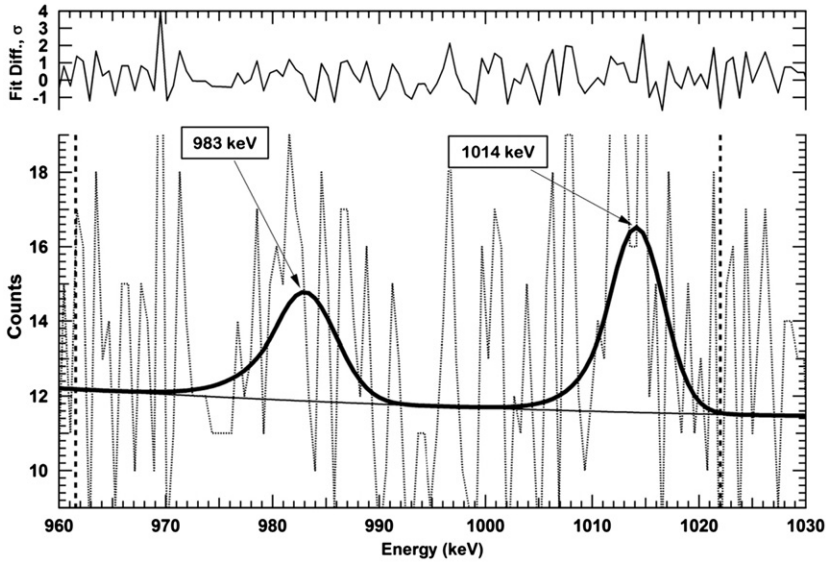

Fig. 9. Fit of the Ti 983 keV and Al 1014 keV peaks to the M2 GRS closest-approach (<2500 km altitude) spectrum. Peaks are fit to the region between the vertical dashed lines with the same peak parameters as those used in Fig. 8. The baseline is fit to a larger region not shown in this figure. Other particulars are as in Fig. 6.

Table 1
Results of gamma-ray peak analysis for Ti, Al, Fe, Si, ^{40}K, and ^{232}Th.

Peak energy (keV)	Pre-CA counts	Pre-CA cpm	CA counts	CA cpm	CA-2[a] pre-CA cpm	CA-2[a] pre-CA average cpm
M1: Ti 983	1572 ± 116	0.735 ± 0.054	43.2 ± 16.0	1.96 ± 0.73	0.49 ± 0.75	0.22 ± 0.52
M2: Ti 983	1664 ± 111	0.843 ± 0.056	39.1 ± 16.9	1.63 ± 0.70	-0.06 ± 0.72	
M1: Al 1014	2228 ± 118	1.041 ± 0.055	55.1 ± 16.1	2.50 ± 0.73	0.42 ± 0.74	0.11 ± 0.52
M2: Al 1014	2035 ± 103	1.030 ± 0.052	44.4 ± 16.1	1.85 ± 0.67	-0.21 ± 0.68	
M1: Fe 847	1234 ± 117	0.577 ± 0.055	49.2 ± 15.4	2.24 ± 0.70	1.09 ± 0.72	1.05 ± 0.52
M2: Fe 847	1158 ± 129	0.586 ± 0.065	52.4 ± 17.9	2.18 ± 0.74	1.01 ± 0.76	
M1+M2: Si 1779	1095 ± 133	0.266 ± 0.032	157 ± 21	3.41 ± 0.46	2.88 ± 0.46	
M1+M2: K 1461	1038 ± 86	0.252 ± 0.021	34.9 ± 11.6	0.76 ± 0.25	0.51 ± 0.26[a]	
M1+M2: Th 2615	289 ± 67	0.070 ± 0.016	23.3 ± 10.9	0.50 ± 0.24	0.43 ± 0.24[a]	

Notes: Pre-CA denotes pre-flyby high-altitude background, and CA denotes closest approach (less than 2500 km altitude). cpm is counts per minute. Accumulation times are M1 pre-CA=2140 min, M1 CA=22 min, M2 pre-CA=1975 min, M2 CA=24 min.

[a] For K and Th, this column is given by CA–pre-CA (because no background amplification is present for radioisotopes). Errors are 1σ.

Brückner and Masarik (1997) for instance, would decrease the factor only by ~5%, however.

An additional potential source of systematic uncertainty is the assumption that the amplification factor is the same for the different elements considered. However, calculations of Ti, Fe, and Si background amplification factors from NS flyby spectra multiplied by their respective inelastic cross-sections indicate that the NS flyby spectra change somewhat with altitude but that the Ti and Fe factors are only a few percent higher than that for Al and the Si factor is a few percent lower, which might be expected since Fe and Ti have a lower inelastic scattering reaction energy threshold than Al, whereas Si has a higher threshold. Thus a background amplification factor value of 2 is used below for Ti, Fe, and Si, with no consideration of count statistical or systematic error in the value. The virtue of these experimentally derived background amplification factors is that they account for some complicated normalization variations with spacecraft altitude and attitude using simple calculations that would be difficult and time-consuming to model accurately. Note that these background amplification factors are not unique; their values will be different for different altitude ranges used to average the closest-approach spectra, for example, since the amount of background in the closest-approach spectra varies with altitude. Taking the background amplification factor to be 2, the M1 and M2 spectral analysis of the Ti 984-keV peak yields 0.22 ± 0.52 counts/min for the net count rate averaged over the two flybys, not considering errors in background amplification. The statistical uncertainty in the net count rate is too large to distinguish net count rates

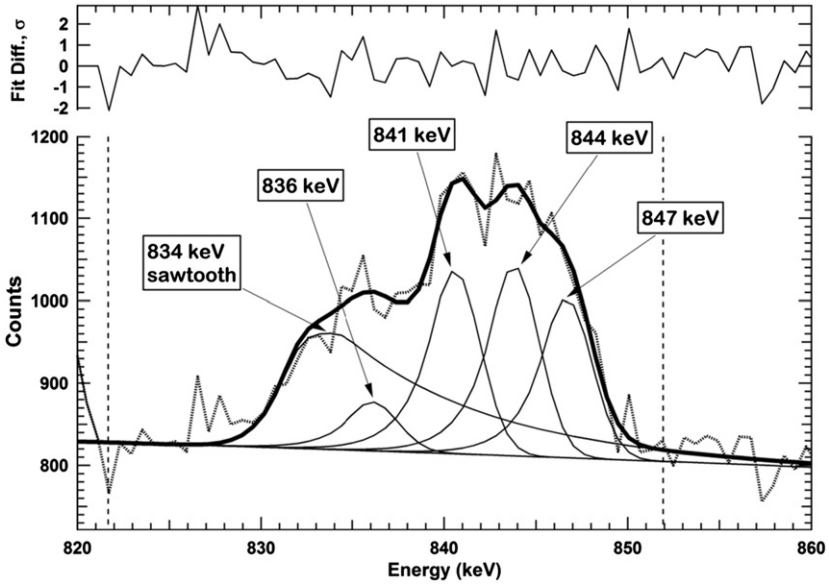

Fig. 10. Fit of four peaks including the Fe peak at 847 keV to the M1 high-altitude GRS background spectrum. The other three peaks are due to activation of material near the detector. These peaks are superimposed on a "sawtooth" feature at 834 keV due to fast neutron interactions in the detector. In all fits, the thick solid black line denotes the full fit (sum of all peaks and the baseline), and the thin solid lines denote the individual peaks. Peaks are fit to the region between the vertical dashed lines. The baseline is fit to the regions from the vertical dashed lines outward to energies not shown here. Other particulars are as in Fig. 6.

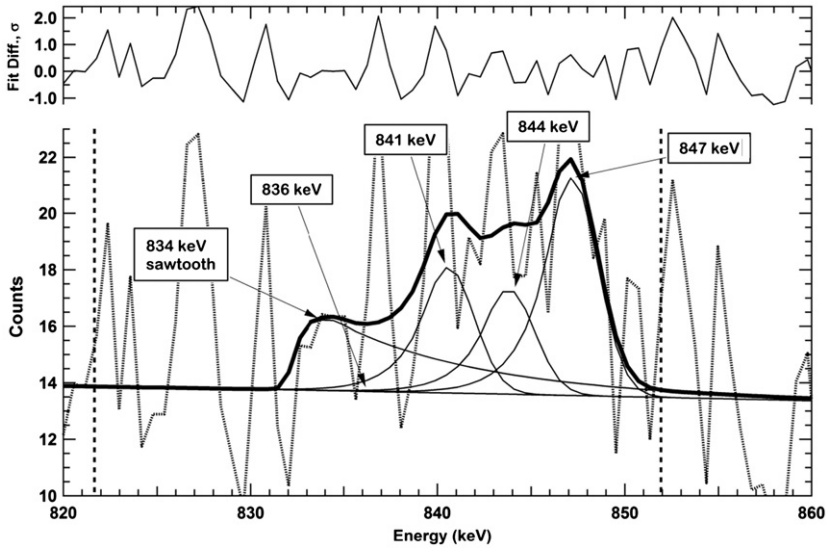

Fig. 11. Fit of four peaks including the Fe peak at 847 keV to the M1 GRS closest-approach (< 2500 km altitude) spectrum. Peaks are fit to the region between the vertical dashed lines with the same peak shape parameters as those used in Fig. 10. The baseline is fit to the regions from the vertical dashed lines outward to energies not shown here. Other particulars are as in Fig. 6.

between the flybys. For Ti, the uncertainty is considerably larger than the average count rate, so it cannot be said that Ti was actually detected, but an upper bound on Ti abundance can be determined.

The GRS spectra prior to and during M1 closest approach for the energy region of the 847-keV Fe peak are shown in Figs. 10 and 11, respectively. The corresponding spectra for M2 are shown in Figs. 12 and 13. Here the Fe 847-keV peak has interference from three peaks generated in the GRS and surrounding spacecraft material: a 844-keV Al peak (from ^{27}Mg), a 840-keV ^{54}Mn peak (electron capture with K-shell binding energy, 312-day half-life), and a 836-keV ^{54}Mn peak (L-shell binding energy). These four peaks sit atop a broad 834-keV Ge sawtooth-shape inelastic-scattering peak, whose shape is characteristic of neutron inelastic scattering occurring inside the Ge detector (Brückner et al., 1987). The count-rate analysis obtained from the peaks shown in Figs. 11–14 is given in Table 1. Taking 2 as the amplification factor, the M1 and M2 spectral analysis of the 847-keV Fe peak yields 1.05 ± 0.52 counts/min for the net count rate averaged over the two flybys. Again, the statistical uncertainties in the net count rates are too large to distinguish net count rates between the flybys, and no error in background amplification factor is considered.

The pre-flyby and flyby spectra for the energy region of the 1779-keV Si peak averaged over the respective altitude ranges for M1+M2 are shown in Figs. 14 and 15. The 1809-keV peak is included in the fit to extend the baseline and thus improve count statistics; this peak comes from ^{26}Al, which has a 7.17×10^5-yr half-life, and from Al inelastic scattering. With 2 as the background amplification factor, a net Si count rate averaged over the flybys of 2.88 ± 0.46 counts/min is obtained from Table 1. (Small contributions to the Si peak from Al inelastic scattering and from ^{28}Al, which has a 2.24-min half-life, are ignored.)

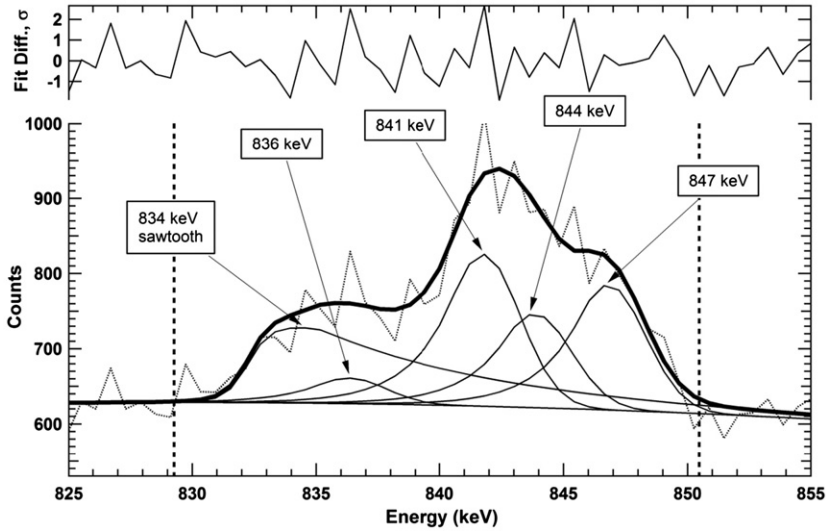

Fig. 12. Fit of four peaks including the Fe peak at 847 keV to the M2 high-altitude GRS background spectrum. The other three peaks are due to activation of material near the detector. These peaks are superimposed on a "sawtooth" feature at 834 keV due to fast neutron interactions in the detector. Peaks are fit to the region between the vertical dashed lines. The baseline is fit to the regions from the vertical dashed lines outward to energies not shown here. Other particulars are as in Fig. 6.

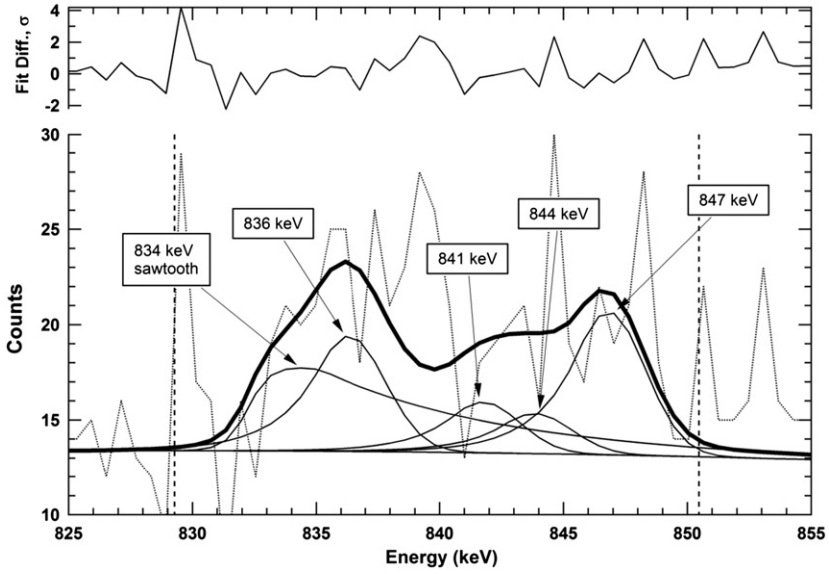

Fig. 13. Fit of four peaks including the Fe peak at 847 keV to the M2 GRS closest-approach (<2500 km altitude) spectrum. Peaks are fit to the region between the vertical dashed lines with the same peak shape parameters as those used in Fig. 12. The baseline is fit to the regions from the vertical dashed lines outward to energies not shown here. Other particulars are as in Fig. 6.

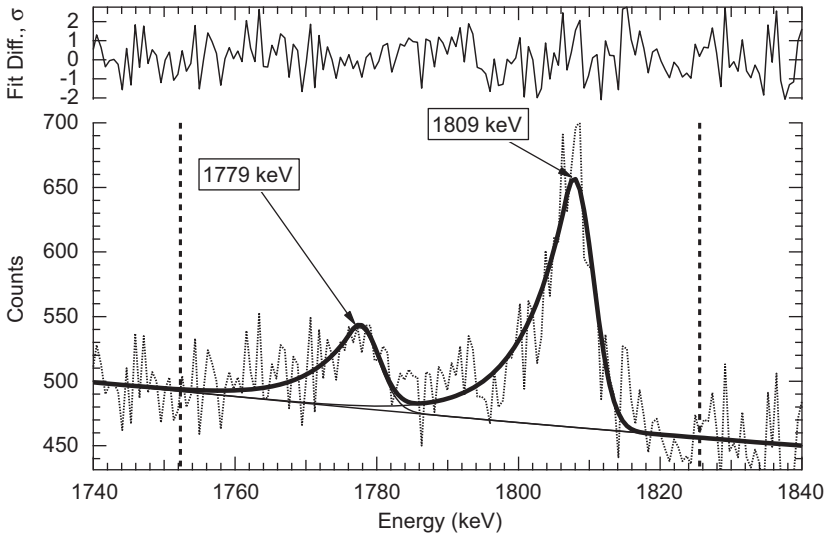

Fig. 14. Fit of the Si 1779 keV and Mg 1809 keV peaks to the sum of the high-altitude GRS background spectra from the first and second Mercury flybys. Peaks are fit to the region between the vertical dashed lines. The baseline is fit to a larger region not shown in this figure. Other particulars are as in Fig. 6.

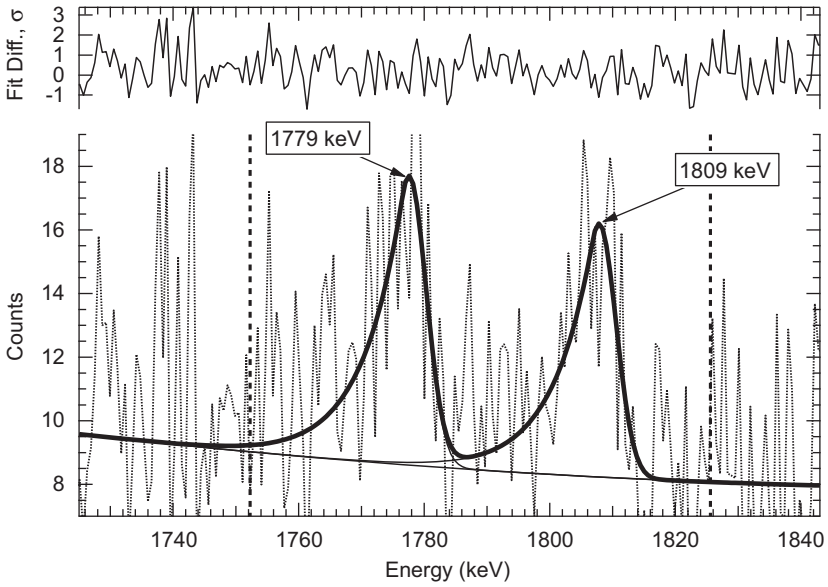

Fig. 15. Fit of the Si 1779 keV and Mg 1809 keV peaks to the sum of the M1 and M2 GRS closest-approach (<2500 km altitude) spectra. Peaks are fit to the region between the vertical dashed lines with the same peak shape parameters as those used in Fig. 14. The baseline is fit to a larger region not shown in this figure. Other particulars are as in Fig. 6.

The pre-flyby and flyby spectra for the energy region of the 1461-keV ^{40}K peak averaged over the respective altitude ranges for M1+M2 are shown in Figs. 16 and 17. A peak at 1454 keV (possibly from Ni inelastic scattering in the spacecraft) overlaps this ^{40}K peak. From Table 1, a net ^{40}K count rate of 0.51 ± 0.26 counts/min is obtained as an average for the two flybys. Shown in Figs. 18 and 19 are the pre-flyby and flyby spectra for the energy region of the 2615-keV ^{232}Th peak averaged for M1+M2. The overlapping peak at 2601 keV is from Fe inelastic scattering. From Table 1, a net ^{232}Th count rate of 0.43 ± 0.24 counts/min is obtained as an average for the two flybys.

5. Determination of elemental abundances from count rates

The only transport computation in the literature predicting Mercury surface gamma-ray emissions due to GCR interactions is that of Brückner and Masarik (1997). The assumed elemental compositions used in these calculations were based on models of Mercury's mantle, not on crustal materials formed by partial melting of mantle source regions, and as a result were not seen as likely to be close to the true composition. We thus set up and performed our own radiation transport computations, with the MCNPX code (McKinney et al., 2006), of gamma-ray emissions from Mercury due to GCR interactions for a given model of elemental abundances that can be adjusted to fit spectral observations.

These gamma-ray emissions are then propagated to the detector at all flyby spacecraft attitudes and altitudes by an efficiency map that properly accounts for the Ge detector efficiency and GRS and spacecraft attenuation for all energies of interest for all orientations that occurred. This efficiency map is based on an energy-efficiency calibration up to 10 MeV at off-nadir angles up to 68° that was conducted at a nuclear reactor using Cl and Cr neutron capture targets, as well as ^{56}Co, ^{226}Ra, and ^{228}Th radioactive sources. This map was extended up to 130° off-nadir angle by interfacing a GEANT4 transport code simulation

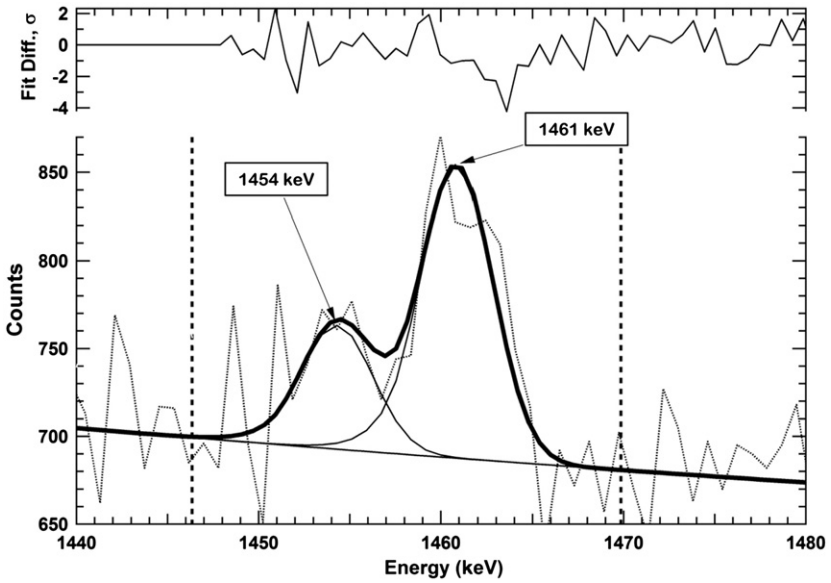

Fig. 16. Fit of the ^{60}Ni 1454 keV and ^{40}K 1461 keV peaks to the sum of the M1 and M2 high-altitude GRS background spectra. Peaks are fit to the region between the vertical dashed lines. The baseline is fit to a larger region not shown in this figure. Other particulars are as in Fig. 6.

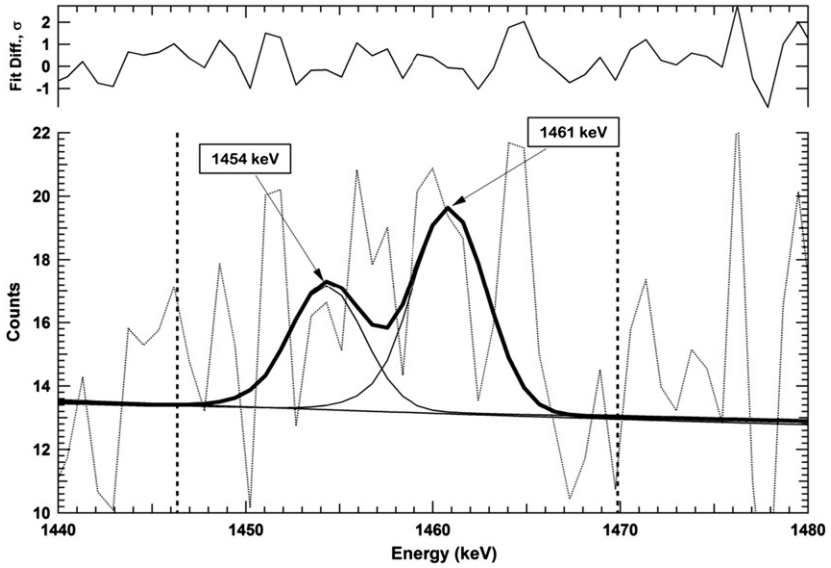

Fig. 17. Fit of the ^{60}Ni 1454 keV and ^{40}K 1461 keV peaks to the sum of the M1 and M2 GRS closest-approach (<2500 km altitude) spectra. Peaks are fit to the region between the vertical dashed lines with the same peak shape parameters as those used in Fig. 15. The baseline is fit to a larger region not shown in this figure. Other particulars are as in Fig. 6.

(Agostinelli et al., 2003) to a computer-aided design (CAD) model of element attenuations for the spacecraft and the instruments. The GEANT4 computation faithfully reproduced the experiment calibration efficiencies. Errors in this computation are estimated to be only a few percent and are not considered in determining abundance errors.

In principle, if the change in gamma-ray peak fluxes caused by variations in GCR flux magnitude and spectrum during the flybys, relative to the GCR flux magnitude and spectrum used in our MCNPX computations, is known, elemental abundances can then be calculated directly from our data. Unfortunately, our best measure of spacecraft GCR flux is probably the charge-reset rate of the GRS borated-plastic shield, but because the GRS was on only during the flybys and during initial commissioning (which occurred during a major solar flare), we currently do not have a good calibration of absolute spacecraft GCR flux magnitude. Nor do we currently have an accurate way of correcting gamma-ray peak fluxes for changes in the GCR spectrum caused by solar activity. Without an ability to normalize our experiment gamma-ray peak fluxes to account properly for variations in GCR flux, and in cognizance of the substantial uncertainties in our other normalizations mentioned above, we decided that our elemental abundance uncertainties would be minimized by determining a best value for Si abundance from cosmochemical arguments and then normalizing our gamma-ray fluxes to yield this Si abundance. This strategy was adopted because the average surface Si abundance for a rocky terrestrial planet is likely to vary over only a relatively narrow range compared to our abundance uncertainties.

To sharpen the range in Si abundances for the surface of Mercury, we consider possible lunar analogs for surface composition, given the likelihood that surface composition on Mercury, as on the Moon (and all terrestrial planets), differs from bulk silicate

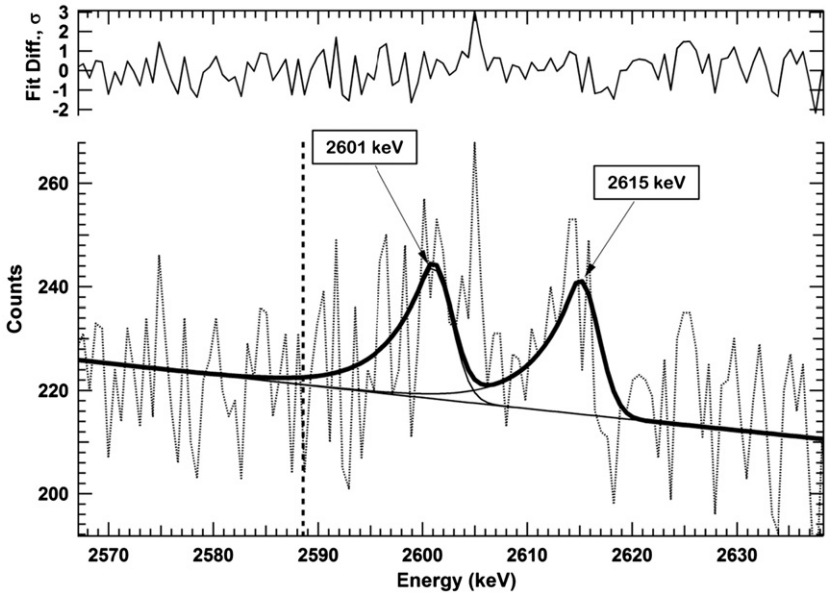

Fig. 18. Fit of an overlapping peak and the ^{232}Th peak at 2615 keV to the sum of the M1 and M2 high-altitude GRS background spectra. Peaks are fit to the region between the vertical dashed lines. The baseline is fit to a larger region not shown in this figure. Other particulars are as in Fig. 6.

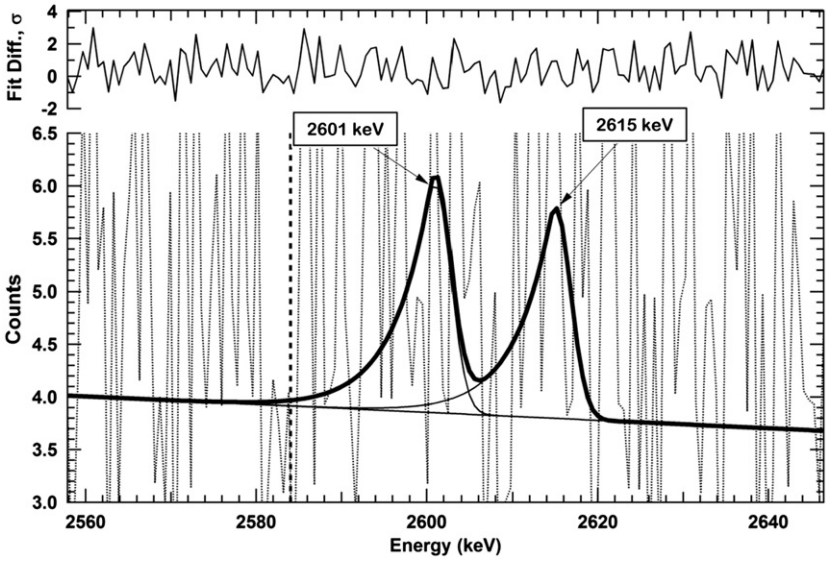

Fig. 19. Fit of an overlapping peak and the ^{232}Th peak at 2615 keV to the sum of the M1 and M2 GRS closest-approach (<2500 km altitude) spectra. Peaks are fit to the region between the vertical dashed lines with the same peak shape parameters as those used in Fig. 18. The baseline is fit to a larger region not shown in this figure. Other particulars are as in Fig. 6.

composition. The range of Si in lunar volcanic rocks is ~17–24% (Papike et al., 1998). This range includes average Si values for high-Ti basalts, high-Ti picritic glasses (which are low in Si), pigeonite basalts, olivine basalts, Apollo 12 ilmenite basalts, very high-K basalts, high-Al basalts, very low Ti basalts, ferroan anorthosites, Mg-rich plutonic rocks, alkali rocks, quartz monzodiorites (which have high Si values), and KREEP basalts. Among lunar basalts (excluding the high-Ti variety), the average Si value is 21.5 ± 1.1%. For comparison, ground-based mid-infrared observations of the transparency minimum known to be diagnostic of SiO_2 abundance in silicates indicate a range for Mercury of 17–21 wt% Si (Boynton et al., 2007). It is worth noting that some magma ocean crystallization models for Mercury (Brown and Elkins-Tanton, 2009) produce much higher Si concentrations, including the possibility of a quartz-dominated flotation crust. However, these models are based on a particular, Si-rich starting composition, which may not be applicable. As constrained by color and spectral observations of Mercury, the equilibrium and fractional crystallization models of Stockstill-Cahill and McCoy (2010) suggest that compositions based on those of lunar high-Ti picritic glasses (but with reduced FeO abundances) may be a possible starting magma composition for volcanic material on Mercury's surface. End products of such magmas must be capable of satisfying the lack of a spectral absorption feature attributable to FeO in Mercury's surface silicates (McClintock et al., 2008); the need for a spectrally neutral opaque phase as a constituent of intermediate terrain, low-reflectance blue plains, and low-reflectance material (Denevi et al., 2009); and the Fe+Ti abundances inferred from MESSENGER NS observations (Lawrence et al., 2010). High-Ti lunar picritic glasses have an average Si of 17.3 ± 0.9% (Papike et al., 1998). On the basis of all of these considerations, we chose a value of 18% Si abundance for normalization.

Table 2
Elemental abundance analysis results (1–σ uncertainty).

Peak energy (keV)	Average cpm	Model cpm	Model abundance (wt%)	Mercury abundance (wt%)	$2-\sigma$ Upper limit (wt%)
Si 1779	2.88 ± 0.46	2.93	18.0	18.0 ± 2.9	23.8
Ti 983	0.22 ± 0.52	0.66	3.6	1.2 ± 2.9	7.0
Fe 847	1.05 ± 0.52	1.25	5.7	4.9 ± 2.4	9.7
K 1461	0.51 ± 0.26	1.03	0.087	0.043 ± 0.022	0.087
Th 2615	0.43 ± 0.24	0.538	1.30	1.04 ± 0.58	2.2

We chose element abundances for our MCNPX computations that approximately matched the count rates seen in the analyses in Table 1, except that we chose a Si abundance of 18%. Our efficiency map calculations summed over the spacecraft attitudes and altitudes less than 2500 km then yield an expected count rate for our model. The element abundance parameters that follow from this choice are shown in Table 2. The net flyby gamma-ray count rates, expressed as counts per min (cpm), for the elements with gamma rays from neutron inelastic scattering (Si, Ti, and Fe) are multiplied by the model abundance, divided by the model-expected cpm, and multiplied by the ratio of Si model-expected cpm to Si flyby cpm, to obtain the Mercury abundance in the fifth column. The ratio of Si model-expected cpm to Si flyby cpm accounts for GCR normalization (and any other linear normalization) required to yield a Si abundance of 18%. Abundances of the radioactive elements (K and Th) are obtained in the same way, but multiplication by the ratio of Si model-expected cpm to Si flyby cpm is not needed. Upper bounds on abundances at the $2-\sigma$ (95% confidence) level are shown in the last column of Table 2. These abundance uncertainties are derived only from count statistics, so no errors in background amplification factor are included.

The goal of this paper is to determine preliminary elemental abundances for Mercury surface material from GRS flyby observations prior to MESSENGER's insertion into orbit about Mercury, and the discussion below is based on these preliminary results. However, there is ongoing work that will improve both the analysis reported here for the flybys and the analysis of data that will be obtained during the Mercury orbital mission phase. Normalizations will include a small dead-time correction using a pulser (Goldsten et al., 2007) and correction for cosmic-ray flux variation obtained from the GRS shield charge-reset rate (backed up by the NS cosmic-ray mode rate) (Goldsten et al., 2007). When available, these calibrations can be used to improve the flyby results as well as the orbital observations. Improved background amplification factors for both fast and thermal neutron reactions, with substantially improved count statistics, are expected from firmware that provides pulse-shape analysis for the Ge detector borated-plastic shield, when in coincidence with the 478-keV B gamma-ray detected by the Ge. This firmware has been uploaded to the detector (but was unavailable for the flybys and thus cannot be used to improve the flyby background amplification factors).

6. Discussion and conclusions

Of the elements studied here, only Si has a gamma-ray flux that is clearly resolved from background by more than 3σ (greater than 99% detection probability) and thus can be considered a firm detection (see Table 2). The fluxes of Fe and K are significant only at $\sim 2\sigma$ (95% detection probability) and that of Th at 1.8σ (88% detection probability). The Ti flux, considering its large relative standard deviation, is consistent with little or no Ti on the planetary surface. We can establish only an upper bound on Ti abundance, 7 wt% at the $2-\sigma$ level. The statistical errors in K and Th abundances are too great to estimate the K/Th abundance ratio. The absolute abundance estimates of Fe and Ti are tied to an assumed Si abundance of 18% and would thus change proportionally if the Si abundance is different from this figure. In this regard, forming abundance ratios with respect to Si helps reduce systematic errors that are of similar magnitude for the analyzed elements. The ratios of Fe and Ti to Si are 0.27 ± 0.14 and 0.07 ± 0.16, respectively ($1-\sigma$ errors). Relative abundance values are likely to be somewhat more robust than the estimated absolute abundances.

A comparison of these derived Fe/Si and Ti/Si ratios ($2-\sigma$ upper bounds in the shaded area) to those measured in lunar samples (squares), predicted for Mercury surface lavas (circles), and calculated for compositions with Fe and Ti dominated by the mineral ilmenite, $FeTiO_3$ (diamonds), is shown in Fig. 20. Within the considerable range of uncertainties in these values, a wide range of interpretations is permissible, although some compositions (e.g., FeO-rich basaltic compositions akin to Apollo 11 and Luna 16 and 24) are excluded. The exclusion of these latter compositions is not surprising given the general lack of evidence for a 1 μm absorption feature from FeO in silicates in reflectance spectra of Mercury (Boynton et al., 2007).

Fluxes of thermal neutrons measured by MESSENGER's NS during the three Mercury flybys (Lawrence et al., 2010) indicate a relatively high abundance of neutron-absorbing elements, interpreted as most likely consisting of some combination of Fe and Ti. The inferred neutron absorption cross-section is broadly consistent with that produced by soils returned by the Luna 16, 20, and 24 missions, although the apparent lack of FeO in silicates at Mercury's surface led Lawrence et al. (2010) to suggest a high abundance of Fe–Ti oxides, consistent with earlier interpretations of color observations (Denevi et al., 2009). If the observed neutron absorption is due to Fe and Ti in ilmenite, for instance, the NS data are consistent with ilmenite abundances of 7–18% (Lawrence et al., 2010). The GRS-derived upper bounds on Fe/Si and Ti/Si ratios are consistent with this range (Fig. 20) and would allow additional Fe or FeO in the form of nanophase iron and/or FeO in silicates, although petrologic modeling suggests that FeO in silicates would be incompatible with the presence of FeO-rich ilmenite (Riner et al., 2010). The GRS errors, although large, also allow for a similar

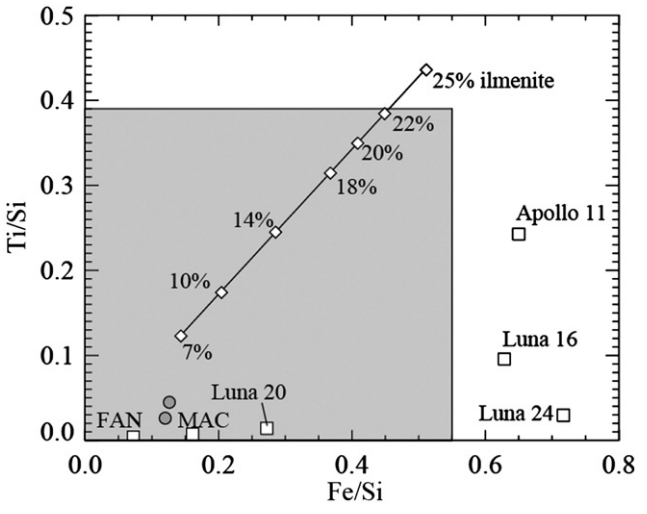

Fig. 20. Fe/Si and Ti/Si ratios derived from MESSENGER flyby GRS data (shaded area, which includes $2-\sigma$ errors) compared with lunar and possible Mercury compositions. Filled circles are model compositions of surface lavas (Taylor and Scott, 2004). Squares are lunar samples, including a ferroan anorthosite, FAN (Lawrence et al., 2010), and lunar meteorite MacAlpine Hills 88105 (MAC), a lunar anorthositic breccia (Jarosewich, 1990). Diamonds are calculated ratios for compositions with indicated abundances of ilmenite (wt%) and an assumed bulk Si abundance of 18 wt%.

range of ilmenite abundances (from ~7 to ~20 wt% to reach the $2-\sigma$ upper limits, Fig. 20), consistent with the conclusions of Denevi et al. (2009) and Lawrence et al. (2010). If instead of ilmenite, the rhombic oxide geikeilite ($MgTiO_3$) is present (Riner et al., 2010), the mixing line in Fig. 20 would shift to the left to lower Fe/Si values. Such a possibility is entirely permissible within the uncertainties of the measurements presented here.

Within uncertainties, the Fe/Si and Ti/Si values presented here are also consistent with low abundances of Fe and Ti on the surface of Mercury. Although other evidence (e.g., abundances of neutron absorbers; Lawrence et al., 2010) seem to preclude a feldspar-rich crust, basaltic to ultramafic compositions (Taylor and Scott, 2004) derived from partial melting of Bencubbin-like or enstatite-chondrite-like metal-rich, low-FeO material or magma ocean crystallization products (Brown and Elkin-Tanton, 2009) are permissible. Under such a scenario, an alternative neutron absorber to Fe and/or Ti would have to be present on the surface of Mercury.

The small upper bound on K (<0.09 wt%) obtained from the flyby data already can rule out some suggested surface compositions. Sprague et al. (2009) used linear combinations of laboratory spectral measurements to fit telescopic mid-infrared spectra of Mercury and infer the mineralogy of three surface regions. On the basis of earlier spectral data, the regions observed telescopically were inferred to have K contents ranging up to 1.3 wt% (Nittler et al., 2008). Among areas viewed telescopically, a region of dark plains (low-reflectance blue and intermediate plains) to the west-southwest of the Caloris basin provides the closest analog to areas sampled by the GRS during the Mercury flybys. This region lacked potassium feldspar in the best-fit solutions, consistent with the upper limit of K measured by GRS during the flybys. Although one might be tempted to infer a volatile-poor composition from these observations, Sprague et al. (2009) suggested that the moderately volatile element sodium is present as Na-rich plagioclase feldspar, albite, and other minor Na-bearing minerals. Even the inferred low abundance of K might be local, as high-reflectance red plains of the Caloris basin interior were inferred to contain higher abundances of K. An important future measurement for the GRS will be to determine spatial variations in the abundances of Na, K, and other volatile lithophile elements on Mercury and their relationship to plains units.

This work demonstrates that the MESSENGER Gamma-Ray Spectrometer is functioning as designed and is capable of identifying and determining the abundances of surface elements on Mercury. The narrow energy resolution of the high-purity Ge detector is crucial for analysis of the Fe spectral region, for resolving overlapping peaks, and for reducing background. During MESSENGER's orbital mission phase, GRS data analysis will be similar to flyby analysis because the orbits are highly elliptical, with a periapsis altitude of 200–500 km and a ~15,000-km apoapsis altitude. The many passes over the planetary surface from orbit should culminate in substantially more precise estimates of the abundances of Si, Fe, Ti, K, and Th, as well as other elements, particularly at mid to high northern latitudes. Further work will be required to determine the best definition of background amplification factors and the errors involved.

Acknowledgments

Several of the authors acknowledge support from NASA's MESSENGER Participating Scientist Program. The MESSENGER project is supported by the NASA Discovery Program under contracts NASW-00002 to the Carnegie Institution of Washington and NAS5-97271 to the Johns Hopkins University Applied Physics Laboratory.

References

Agostinelli, S., et al., 2003. GEANT4—a simulation toolkit. Nucl. Instrum. Meth. A 506, 250–303.

Boynton, W.V., Sprague, A.L., Solomon, S.C., Starr, R.D., Evans, L.G., Feldman, W.C., Trombka, J.I., Rhodes, E.A., 2007. MESSENGER and the chemistry of Mercury. Space Sci. Rev. 131, 85–104.

Brown, S.M., Elkins-Tanton, L.T., 2009. Composition of Mercury's earliest crust from magma ocean models. Earth Planet. Sci. Lett. 286, 446–455.

Brückner, J., Masarik, J., 1997. Planetary gamma-ray spectroscopy of the surface of Mercury. Planet. Space Sci. 45, 39–48.

Brückner, J., Wänke, H., Reedy, R.C., 1987. Neutron-induced gamma-ray spectroscopy: simulations for chemical mapping of planetary surfaces. Proc. Lunar Planet. Sci. Conf. 17th, Part 2, J. Geophys. Res. 92, E603–E616.

Denevi, B.W., Robinson, M.S., Solomon, S.C., Murchie, S.L., Blewett, D.T., Domingue, D.L., McCoy, T.J., Ernst, C.M., Head, J.W., Watters, T.R., Chabot, N.L., 2009. The evolution of Mercury's crust: a global perspective from MESSENGER. Science 324, 613–618.

Evans, L.G., Rhodes, E.A., Goldsten, J.O., Nittler, L.R., Starr, R.D., McCoy, T.J., Sprague, A.L., Boynton, W.V., Solomon, S.C., 2008. Gamma-Ray Spectrometer measurements at Mercury during MESSENGER's first two flybys. Eos Trans. Am. Geophys. Un. 89 (53) (Fall Meeting Suppl., abstract U21A-0028).

Goldsten, J.O., Rhodes, E.A., Boynton, W.V., Feldman, W.C., Lawrence, D.J., Trombka, J.I., Smith, D.M., Evans, L.G., White, J., Madden, N.W., Berg, P.C., Murphy, G.A., Gurnee, R.S., Strohbehn, K., Williams, B.D., Schaefer, E.D., Monaco, C.A., Cork, C.P., Eckels, J.D., Miller, W.O., Burks, M.T., Hagler, L.B., DeTeresa, S.J., Witte, M.C., 2007. The MESSENGER Gamma-Ray and Neutron Spectrometer. Space Sci. Rev. 131, 339–391.

Jarosewich, E., 1990. Chemical analyses of meteorites—a compilation of stony and iron meteorite analyses. Meteoritics 25, 323–338.

Lawrence, D.J., Feldman, W.C., Goldsten, J.O., McCoy, T.J., Blewett, D.T., Boynton, W.V., Evans, L.G., Nittler, L.R., Rhodes, E.A., Solomon, S.C., 2010. Identification and measurement of neutron-absorbing elements on Mercury's surface. Icarus 209, 179–194.

McClintock, W.E., Bradley, E.T., Vervack, R.J., Killen, R.M., Sprague, A.L., Izenberg, N.R., Solomon, S.C., 2008. Mercury's exosphere: observations during MESSENGER's first flyby. Science 321, 62–65.

McKinney, G.W., Lawrence, D.J., Prettyman, T.H., Elphic, R.C., Feldman, W.C., Hagerty, J.J., 2006. MCNPX benchmark for cosmic ray interactions with the Moon. J. Geophys. Res. 111, E06004. doi:10:1029/2005JE002551.

Nittler, L.R., Evans, L.G., McCoy, T.J., Sprague, A.L., Boynton, W.V., Donaldson Hanna, K.L., Goldsten, J.O., Rhodes, E.A., Schlemm II, C.E., Solomon, S.C., Starr, R.D., 2008. X-Ray and Gamma-Ray Spectrometer observations of the elemental composition of the equatorial region of Mercury: testing formation models. Lunar Planet. Sci. 39 (abstract 1205).

Papike, J.J., Ryder, G., Shearer, C.K., 1998. Lunar samples. Rev. Mineral. Geochem. 36, 5.01–5.234.

Reedy, R.C., 1978. Planetary gamma-ray spectroscopy. In: Proceedings of the Ninth Lunar and Planetary Science Conference, pp. 2961–2984.

Rhodes, E.A., Evans, L.G., Goldsten, J.O., Starr, R.D., Boynton, W.V., Sprague, A.L., Lawrence, D.J., Solomon, S.C., 2009. Gamma-Ray Spectrometer measurements at Mercury during the MESSENGER flybys. Eos Trans. Am. Geophys. Un. 90 (52) (Fall Meeting Suppl., abstract P21A-1194).

Riner, M.A., McCubbin, F.M., Lucey, P.G., Taylor, G.J., Gillis–Davis, J.J., 2010. Mercury surface composition: integrating petrologic modeling and remote sensing data to place constraints on FeO abundance. Icarus 209, 301–313.

Solomon, S.C., McNutt, R.L., Gold, R.E., Domingue, D.L., 2007. MESSENGER mission overview. Space Sci. Rev. 131, 3–39.

Sprague, A.L., Donaldson Hanna, K.L., Kozlowski, R.W.H., Helbert, J., Maturilli, A., Warell, J.B., Hora, J.L., 2009. Spectral emissitivity measurements of Mercury's surface indicate Mg- and Ca-rich mineralogy, K-spar, Na-rich plagioclase, rutile, with possible perovskite and garnet. Planet. Space Sci. 57, 364–383.

Stockstill-Cahill, K.R., McCoy, T.J., 2010. Petrologic modeling of chondritic parent melts: implications for MESSENGER. Meteorit. Planet. Sci. 45 (Suppl.), A193.

Taylor, G.J., Scott, E.R.D., 2004. Mercury. In: Davis, A.M. (Ed.), Meteorites, Comets, and Planets. Treatise on Geochemistry, vol. 1. Elsevier, Amsterdam, pp. 477–485.